Zitierweise: *Angew. Chem. Int. Ed.* **2025**, *64*, e202504923
doi.org/10.1002/anie.202504923

VIP **Zn-Air Batteries** **Very Important Paper**

Altering the Symmetry of Fe–N–C by Axial Cl-Mediation for High-Performance Zinc–Air Batteries

Mengni Liu[+], Yuxiao Liu[+], Xia Zhang, Linfeng Li, Xinying Xue, Muhammad Humayun, Haowei Yang, Libo Sun, Mohamed Bououdina, Jianrong Zeng, Deli Wang, Rony Snyders, Dingsheng Wang, Xin Wang,* and Chundong Wang**

Abstract: Fe–N–C catalyst is acknowledged as a promising alternative for the state-of-the-art Pt/C in oxygen reduction reaction (ORR) toward cutting-edge electrochemical energy conversion/storage applications. Herein, a "Cl-mediation" strategy is proposed on Fe–N–C for modulating the catalyst's electronic structure toward achieving remarkable ORR activity. By coordinating axial Cl atoms to iron phthalocyanine (FePc) molecules on carbon nanotubes (CNTs) matrix, a Cl-modulated Fe–N–C (FePc-Cl-CNTs) catalyst is synthesized. The as-prepared FePc-Cl-CNTs exhibit an improved ORR activity with a half-wave potential of 0.91 V versus RHE in alkaline solution, significantly outperforming the parent FePc-CNTs (0.88 V versus RHE). The advanced nature of the as-prepared FePc-Cl-CNTs is evidenced by a configured high-performance rechargeable Zn–air battery, which operates stably for over 150 h. The experiments and density functional theory calculations unveil that axial Cl atoms induce the transformation of FePc from its original D_{4h} to C_{4v} symmetry, effectively altering the electrons distribution around the Fe-center, by which it optimizes *OH desorption and subsequently boosts the reaction kinetics. This work paves ways for resolving the dilemma of Fe–N–C catalysts' exploration via engineering Fe–N–C configuration.

Introduction

Oxygen reduction reaction (ORR) plays a pivotal role in rechargeable zinc–air batteries (ZABs), fuel cells, and other applications.[1–3] However, the strong energy of the O—O bond (498 kJ mol^{-1}), along with the complex multielectron transfer process, leads to a sluggish ORR kinetics. This significantly limits the practical applications of electrochemical devices/systems.[4,5] Although platinum-based catalysts (e.g., Pt/C) are considered the best choice for ORR due to their exceptional catalytic activity, their high cost, scarcity, limited stability,[6] and poor tolerance to carbon monoxide/methanol[7,8] limit their large-scale applications. As such, the exploration of cost-efficient nonprecious metal-based catalysts with remarkable catalytic activity is highly desirable. Fe–N–C catalysts have emerged as a promising alternative to conventional metal-based catalysts for ORR because of their high atomic utilization, low cost, and outstanding catalytic performance.[9–11] Among them, FeN_4 configuration is considered ideal for achieving efficient ORR activity because the atomically dispersed Fe–N–C catalyst ensures precise atomic utilization.[5,12] Nonetheless, most

[*] M. Liu[+], X. Xue
Department of Physics, College of Science, Shihezi University, Xinjiang 832003, P.R. China
E-mail: yyingxx@163.com

M. Liu[+], Y. Liu[+], X. Zhang, L. Li, C. Wang
School of Integrated Circuits, State Key Laboratory of New Textile Materials and Advanced Processing, Huazhong University of Science and Technology, Wuhan 430074, P.R. China
E-mail: apcdwang@hust.edu.cn

M. Humayun, M. Bououdina, C. Wang
Energy, Water and Environment Lab, College of Humanities and Sciences, Prince Sultan University, Riyadh 11586, Saudi Arabia

H. Yang
School of Materials Science and Engineering, Central South University, Changsha 410083, P.R. China

L. Sun, X. Wang
Department of Chemistry, City University of Hong Kong, Hong Kong 999077, P. R. China
E-mail: wang.xin@cityu.edu.hk

J. Zeng
Shanghai Synchrotron Radiation Facility, Shanghai Advanced Research Institute, Chinese Academy of Sciences, Shanghai 201204, P.R. China

D. Wang
School of Chemistry and Chemical Engineering, Huazhong University of Science and Technology, Wuhan 430074, P.R. China

R. Snyders
Chimie des Interactions Plasma Surfaces (ChIPS), University of Mons, Mons 7000, Belgium

R. Snyders
Materia Nova Research Center, Mons B-7000, Belgium

D. Wang
Department of Chemistry, Tsinghua University, Beijing 100084, P.R. China

[+] Both authors contributed equally to this work.

Additional supporting information can be found online in the Supporting Information section

Fe–N–C catalysts are mainly synthesized via the pyrolysis pathway, which leads to uneven distribution of active sites, poses the barriers to precisely regulate electronic structures, and not evident to clarify the complex interactions between the support and active centers. In such a kind of prepared Fe–N–C catalysts, both the intrinsic activity and stability of the catalysts were generally deteriorated.[13–17] Thus, formulating catalyst design strategies that can allow for uniform distribution of active sites, precise modulation of electronic structures, and create strong interfacial interactions is particularly crucial for enhancing the catalytic activity as well as stability of Fe–N–C catalysts.[18–22]

Iron phthalocyanine (FePc), a transition metal–nitrogen chelating compound with a well-defined molecular structure, has garnered significant attention due to its intrinsic high ORR activity. Previous research revealed that FePc immobilized on curved carbon-based substrates, such as carbon nanotubes and onion-like carbon,[23] exhibited superior electrochemical performance for ORR.[24] However, on the other hand, FePc suffered from poor electrical conductivity (1.4×10^{-7} to 5.7×10^{-7} S cm^{-1}) and demonstrated a planar symmetric configuration, which resulted in a symmetrical electron distribution around Fe centers, being unfavorable for O_2 adsorption and activation.[25,26] Additionally, due to the planar symmetric structure of FePc, it is prone to dissolve in the solution, leading to metal leaching and finally resulting in poor cycling stability. In light of these facts, finding a novel approach to enhance its ORR performance by modulating the active site structure and overcoming the limitations of its planar conjugated configuration presents a significant challenge yet not well resolved.[22,27–32]

In this work, an innovative "Cl-mediation" strategy is proposed to anchor FePc on CNTs. The as-prepared axial Fe–Cl coordinated catalyst (termed as FePc-Cl-CNTs) demonstrated outstanding ORR performance with a half-wave potential of 0.91 V and a Tafel slope of 33.23 mV dec^{-1}, yielding the ideal four-electron reduction pathway ($n = 3.94$). The advanced feature of the as-prepared FePc-Cl-CNTs could also be evidenced by the configured Zn–air battery (FePc-Cl-CNTs + RuO_2IIZn), delivering an open-circuit voltage of 1.51 V, a maximum power density of 183.5 mW cm^{-2}, and a specific capacity of 797.16 mAh gZn^{-1}. The reason for the observed ORR activity as well as Zn–air battery performance could be due to the fact that the introduced axial Cl atoms (with strong electronegativity) alter the electron distribution of the Fe centers and modulate the splitting of d orbital energy levels of Fe, ensuring the exposure of active sites by disrupting the planar symmetry of FePc. Besides, the introduced Cl atoms enhance the dispersion and stability of active centers by levering defects in carbon framework, which could be another reason for the impressive ORR performance.

Results and Discussion

Synthesis and Characterization

Different from the conventional strategy for randomly forming M–N_x coordination sites on carbon supports via the pyrolysis treatment, a FePc-Cl-CNTs composite was prepared utilizing FePc (a condensed ring aromatic framework and a well-defined molecular structure) as the metal precursor, in which the carbon nanotubes (CNTs) served as the carrier for an extended π conjugated system.[30,33–35] The schematic synthesis process of FePc-Cl-CNTs is displayed in Figure 1a. It involves oxidative acid treatment and the subsequent molten salt engineering (using NaCl as a source for Cl-doping in CNTs). Next, a one-step specific adsorption occurred because of the π–π interaction, and Fe—Cl chemical bond formation allows to anchor FePc molecules. The FePc-Cl-CNTs catalyst was finally formed by a freeze-drying procedure. For comparison, a control sample, a FePc-CNTs catalyst without axial Cl-coordination, was prepared following the same protocol without the addition of NaCl. Detailed synthesis process is illustrated in the Supporting Information.

Scanning electron microscope (SEM) images were recorded to unveil the morphology of the as-prepared samples. As shown in Figure S1, the axial Cl-doped CNTs (Cl-CNTs) display nearly the same morphology as the parent CNTs. The successful introduction of Cl into the framework of CNTs is validated by energy-dispersive X-ray spectroscopy (EDS). The carbon nature of Cl-doped CNTs is confirmed from the recorded powder X-ray diffraction (XRD) patterns, in which the two peaks at 26.1° and 44.1° correspond to the (002) and (101) crystal planes of graphitic carbon.[36] Compared to the pristine CNTs, the introduced Cl caused the (002) peaks of Cl-CNTs being slightly shifted toward lower diffraction angle, signifying the expansion of carbon layer spacing. This shift became more pronounced as the Cl concentration increased (Figure S2). The successful anchoring of Cl on the CNTs can also be evidenced from the Fourier-transform infrared (FTIR) spectroscopy, in which an additional vibrational band at 619 cm^{-1} is observed in the spectra of the Cl-doped CNTs samples,[37] compared to the one of the pristine sample (Figure S3). X-ray photoelectron spectroscopy (XPS) measurement was utilized to evaluate the elemental composition and content of Cl-CNTs and control samples (see Table S1). Compared to pristine CNTs, characteristic peaks at 199.5 and 197.9 eV are discerned in the Cl 2p spectrum, being associated to Cl $2p_{1/2}$ and Cl $2p_{3/2}$ lines (Figure S4).[38–40] These observations evidence the fact that Cl is successfully incorporated into CNTs and form C—Cl bonds on the surface. In addition, the topological defect density of the synthesized metal-free catalyst was quantitatively evaluated using the D_3/G peak area ratio in the Raman spectrum, with the D_3 peak indicating topological defects and the G peak representing the degree of graphitization.[41–43] Compared to the pristine CNTs, a higher D_3/G value (i.e., $D_3/G = 0.952$) is observed in the Cl-CNTs sample (Figure S5), thus suggesting a higher density of inherent defects (similar to sp^3 hybridized carbon) because of the salt effect. Noteworthy, the formed defects ensure decoration of chlorine along axis direction, of which they do not act as the active centers. To verify this conclusion, we prepared CNTs samples with varying degrees of etching and assessed the defect levels by analyzing the I_D/I_G ratio using Raman spectroscopy (Figure S6 (a)). These CNTs samples were then interacted with FePc to obtain a final sample for performance testing

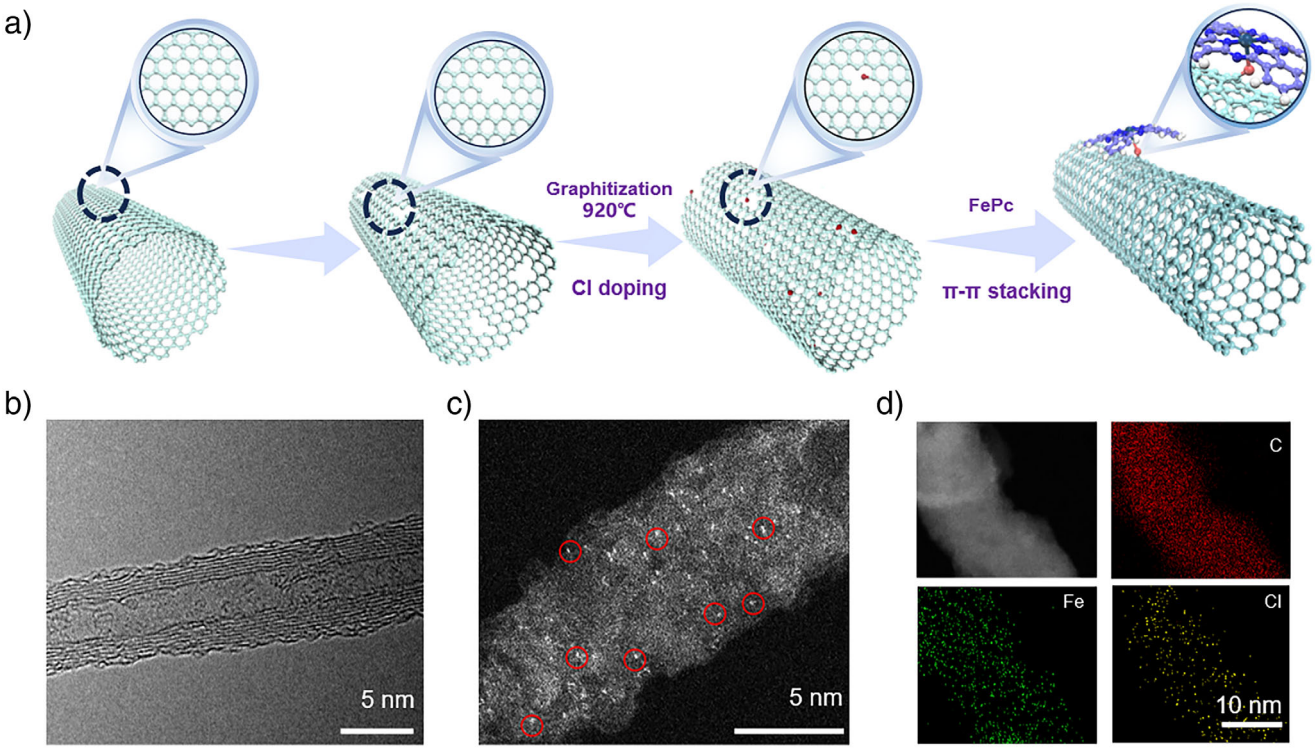

Figure 1. Morphological characterizations of FePc-Cl-CNTs. a) Schematic synthesis process of FePc-Cl-CNTs catalyst. b) TEM image of FePc-Cl-CNTs. c) HAADF-STEM image of FePc-Cl-CNTs showing Fe single atoms (red circles). d) Corresponding EDX mapping image of FePc-Cl-CNTs.

(Figure S6 (b)). The results indicated that the defects did not significantly enhance the catalytic activity.

The as-prepared FePc-Cl-CNTs retained the tubular morphology of the CNTs (Figure S7), and no additional diffraction peaks were identified in the XRD patterns (Figure S8). Also, no Fe clusters or particles were detected as confirmed by transmission electron microscopy (TEM) images (Figures 1b and S9).

To characterize the nanostructure, spherical aberration-corrected high-angle annular dark-field TEM (AC-HAADF-STEM) was further conducted. As anticipated, many bright spots were observed on the CNTs scaffold (Figure 1c), indicating that the Fe atoms were atomically-distributed on the as-prepared FePc-Cl-CNTs. Apart from Fe and C, an additional signal of Cl element was observed in the energy-dispersive X-Ray spectroscopy (EDX) spectrum (Figure S10), again confirming the successful introduction of Cl into CNTs matrix. Complementary XPS analysis further corroborated these findings, quantifying the chlorine content to be 0.59 at. % and providing strong evidence of chlorine's integration within the composite structure (Table S3). All the elements (i.e., C, N, Cl, Fe) are uniformly distributed over the whole CNTs scaffold, as evidenced by elemental mapping shown in Figure 1d. Inductively coupled plasma mass spectrometry (ICP-OES) was utilized to evaluate the amount of atomic-distributed Fe in the samples, which is determined to be 1.08 wt% in FePc-CNTs and 1.16 wt% in FePc-Cl-CNTs (Table S2).

To better understand the chemical states of FePc-Cl-CNTs, XPS analysis was carried out. Apart from the presence of C, N, O, and Fe elements in FePc-CNTs and FePc-Cl-CNTs samples observed from the XPS survey spectrum, an additional Cl peak is identified on FePc-Cl-CNTs (Figure S11), confirming the successful incorporation of Cl atoms into the CNTs in FePc-Cl-CNTs. Figure 2a shows C 1s core-level spectrum, in which the three peaks at 284.8, 285.6, and 289.3 eV correspond to sp^2 carbon, sp^3 carbon, and C–N/Cl, respectively.[44–46] Noteworthy, the ratio of sp^3 content was increased from 33.59% (FePc-CNTs) to 41.68% (FePc-Cl-CNTs), suggesting that a greater number of inherent defects (associated with sp^3 hybridized carbon) was introduced because of Cl-doping, being consistent with the Raman spectroscopy results (Figure 2b). Figure 2c displays the Cl 2p spectrum of FePc-Cl-CNTs, which is deconvoluted into three peaks at 198.2, 200.4, and 201.1 eV, being attributed to the Fe—Cl, Cl $2p_{3/2}$, and Cl $2p_{1/2}$, respectively.[47] The presence of Fe—Cl bond evidences the fact that Cl-CNTs and FePc is chemically bonded rather than merely adsorbed by π–π stacking. Fe 2p spectra of both FePc-Cl-CNTs and FePc-CNTs were recorded as well and shown in Figure 2d. They show that the binding energies of Fe $2p_{1/2}$ and $2p_{3/2}$ in FePc-Cl-CNTs were significantly shifted to higher values compared to those of the FePc-CNTs, signifying that the introduction of Cl results in an electronic delocalization, by which a higher oxidation state of Fe is realized.[48]

In order to gain in-depth insights into the local coordination geometry and electronic state, X-ray absorption near-edge structure (XANES) and extended X-ray absorption fine structure (EXAFS) spectroscopies were performed. As illustrated in Figure 2e, the absorption energy of Fe

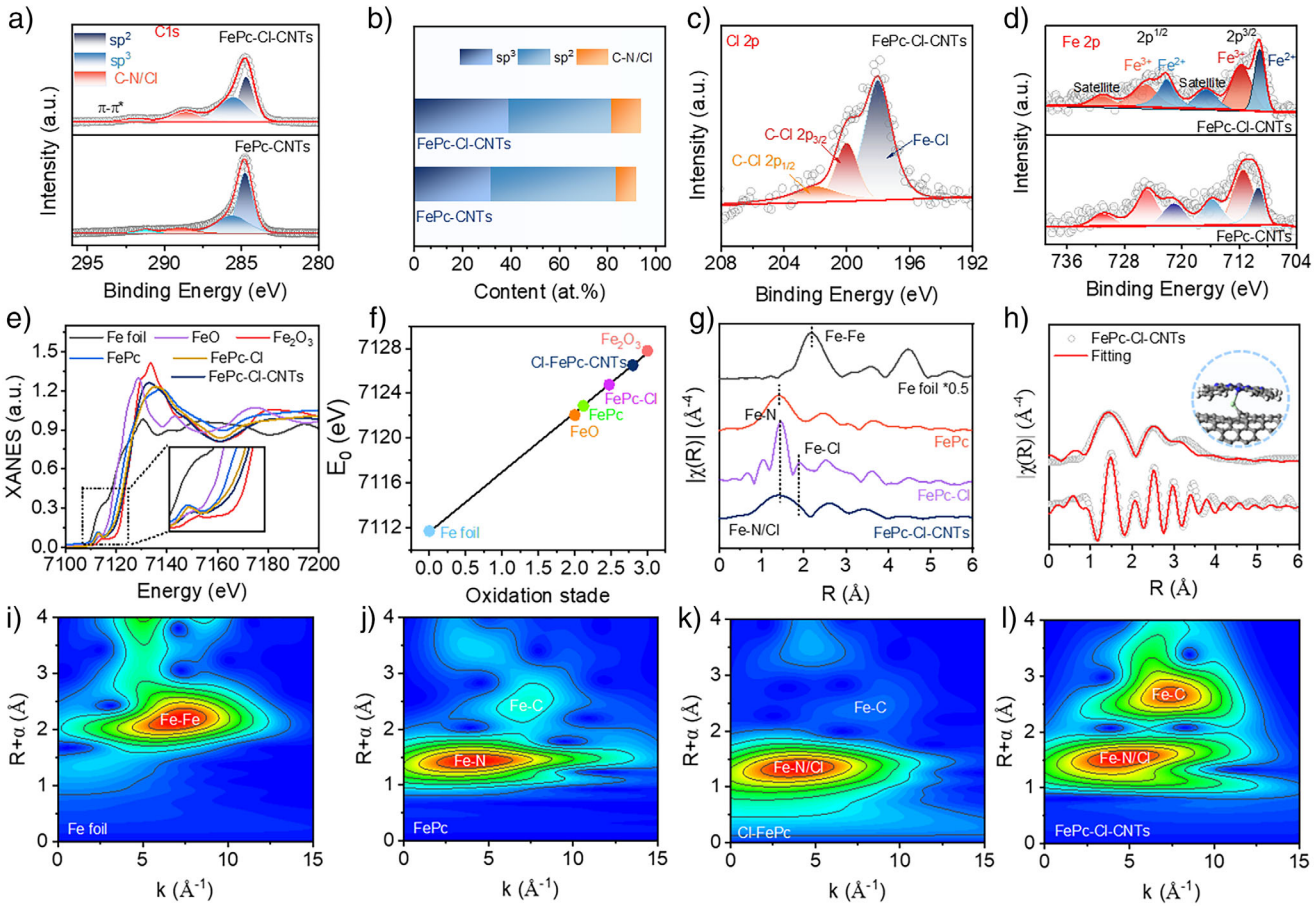

Figure 2. Structure analysis of FePc-Cl-CNTs. a) High-resolution C 1s XPS spectra of FePc-Cl-CNTs and FePc-CNTs. b) Carbon content of sp^2, sp^3, and C-N/Cl in FePc-Cl-CNTs and FePc-CNTs. c) and d) High-resolution Cl 2p and Fe 2p core-level spectra of FePc-Cl-CNTs and FePc-CNTs. e) Normalized Fe K-edge XANES spectra of FePc-Cl-CNTs and the control samples. The inset displays the enlarged K-edge XANES spectra ranging from 7110 to 7125 eV. f) Average iron valence state of the samples. g) Fourier transform of Fe K-edge EXAFS for Fe foil, FePc, Cl-FePc, and FePc-Cl-CNTs. h) Experimental and fitted curves of EXAFS spectra for FePc-Cl-CNTs in R space. Inset shows the model of FePc-Cl-CNTs. (Fe, purple; N, blue; C, gray; Cl, green). i)–l) Wavelet transform plots for Fe foil, FePc, Cl-FePc, and FePc-Cl-CNTs.

K-edge of FePc-Cl-CNTs lies between those of FeO and Fe_2O_3 and is closer to Fe_2O_3, signifying the average valence state of Fe is close to +3. Compared to the control sample FePc, the apparent positive shift of Fe K-edge indicates alteration of the electronic structure of Fe sites, suggesting the valence state of Fe is raised. The reason could be ascribed to the electron transfer to Cl from Fe due to the axial Cl-coordination, which is consistent with the aforementioned XPS observation. In the inset of Figure 2e, reduced peak intensity in the pre-edge (associated with the 1s–4pz electric dipole transition of the planar square D_{4h} configuration) is observed upon Cl-introduction, suggesting a transformation of local symmetry from D_{4h}[49] to C_{4v}.[31,50–53] Of note, such kind of transformation could result in the decrease of freedom in the system and enhances the disruption of the Fe—N_4 planar symmetry. Further analysis of the first derivative of the XANES spectra allows us to calculate the valence state of Fe in the samples (Figure S12). As depicted in Figure 2f, the average valence state of Fe in FePc-Cl-CNTs is determined to be 2.79, which is significantly higher than that of FePc. To elucidate the regulatory mechanisms of catalyst structural symmetry, we examined the dynamics of unpaired electrons using electron paramagnetic resonance (EPR) spectroscopy. As shown in Figure S13, the gradual introduction of chlorine atoms resulted in a significant increase in EPR peak intensity. This notable spectroscopic observation supports an increased population of unpaired electrons within the catalyst, providing compelling evidence for the disruption of crystal symmetry induced by chlorine and the subsequent reconfiguration of the electronic structure. Fourier transform (FT) k^3-weighted EXAFS spectra were plotted as well. As illustrated in Figure 2g, a prominent peak centered at 1.45 Å in R space is observed in sample FePc, which corresponds to the scattering path between Fe and N atoms. Impressively, a significant peak at 1.9 Å is identified in sample FePc-Cl-CNTs, which corresponds to the backscattering between Fe and Cl atoms, further confirming the presence of axial Fe–Cl interactions.[17,21,39] As there is no Fe–Fe fingerprint in the sample FePc-Cl-CNTs, it suggests that Fe atoms are atomically dispersed in the CNTs framework. Furthermore, quantitative least-squares EXAFS curve fitting was conducted to elucidate the coordination of Fe sites. As expected, one

Fe atom is coordinated with four first-shell N atoms (Fe—N_4) in FePc, with an average bond length of 1.93 Å (Figure S14 and Table S4). Different from the case of FePc, it determines that Fe bonds with four first-shell N atoms and one first-shell Cl atom (FeN_4—Cl), with an average bond length of 1.98 Å (where the Fe—N and Fe—Cl bonds are measured to be 1.9 and 2.3 Å, respectively) (Figure 2h). The strong correlation between the measured spectrum and the predicted spectrum of Fe—N and Fe—Cl two-body backscattering signals (χ^2) in K-space further confirms that the major coordination environment of Fe includes Fe—N and Fe—Cl (Figure S15). It should be noted that the collected FT k^3-weighted EXAFS spectra are exactly in line with the simulated EXAFS spectra obtained by using density functional theory (DFT), again supporting the validity of the proposed Cl–Fe–N–C configuration (Figure S16).[54,55] The Cl–Fe–N–C configuration, as well as its monoatomically dispersed nature of Fe, could also be verified from the collected wavelet transform (WT)-EXAFS of FePc-Cl-CNTs and the control samples (Figures 2i–l and S17). The slight variation in the WT-EXAFS of FePc-Cl-CNTs compared to the FePc further indicates that there should exist an interaction between FePc and Cl-CNTs.

Electrocatalytic ORR Performance

The ORR activity of FePc-Cl-CNTs was evaluated in an O_2-saturated 0.1 M KOH electrolyte. All potentials are presented against the reversible hydrogen electrode (RHE). Prior to the ORR performance, cyclic voltammetry (CV) was conducted in a potential range from 0 to 1.1 V versus RHE. Compared to the control sample (FePc-CNTs), the FePc-Cl-CNTs sample delivers a significantly stronger reduction peak (Figure S18), suggesting that the Cl-coordination remarkably increases the intrinsic activity of the catalytic centers. As such, the linear sweep voltammetry (LSV) curves of the samples were then collected. As shown in Figure 3a, the onset potential (E_{onset}) and half-wave potential ($E_{1/2}$) of FePc-Cl-CNTs are 0.98 and 0.91 V versus RHE, respectively, which are superior to those of FePc-CNTs (0.96, 0.88 V) and Pt–C (0.98, 0.86 V). This surpasses the $E_{1/2}$ values of most axially coordinated catalysts prepared under similar conditions reported elsewhere (Figure S19 and Table S6). In addition, we prepared various control samples (Figure S20a) with different chlorine doping ratios and combined them with FePc to evaluate their performance. The results indicate a trend similar to that observed in the precursors, where the combination of a chlorine doping ratio of 1:2 with FePc demonstrates the best oxygen reduction performance (Figure S20b). To further clarify the exceptional electrocatalytic ORR activity of FePc-Cl-CNTs, the corresponding Tafel plots were measured. As depicted in Figure 3c, the Tafel slope of FePc-Cl-CNTs is determined to be 33.23 mV dec^{-1}, outperforming those of FePc-CNTs (41.25 mV dec^{-1}) and the commercial Pt/C (92.1 mV dec^{-1}). It could be attributed to the enhanced reaction kinetics upon Cl-introduction as evidenced from the highest kinetic current density among all the samples (Figure 3b and Table S5). These observations again evidence the role of Cl-coordination in boosting the ORR kinetics of FePc-CNTs. To better understand the electron transfer behaviors in FePc-Cl-CNTs during ORR, polarization curves were collected at different rotation speeds in the range of 400 to 2500 rpm. As demonstrated in Figure S21, the corresponding Koutecky–Levich (K–L) plots (J^{-1} versus $\omega^{-1/2}$) display a strong linear relationship, suggesting that the as-prepared FePc-Cl-CNTs sample follows a first-order reaction kinetics throughout the ORR process. The average number of electrons (n) calculated from the K–L equation is 3.94 within the voltage range of 0.4 to 0.7 V. To further elucidate the electron transfer number (n) and selectivity of the FePc-Cl-CNTs catalyst during the ORR, RRDE measurements were conducted. The yield of H_2O_2 stays below 5%, representing a calculated n value of 3.95 within the potential range of 0.2–0.8 V (Figure 3d), indicating an efficient four-electron transfer process from O_2 to OH^- and a high selectivity of the ORR. Additionally, the turnover frequency (TOF) and mass activity (MA) of FePc-Cl-CNTs at 0.85 V were calculated to be 12.1 s^{-1} and 22.3 A mg^{-1-1}, respectively. These values are significantly higher than those of the FePc-CNTs (8.3 s^{-1} and 14.8 A mg^{-1}) and Pt/C (1.3 s^{-1} and 0.45 A mg^{-1}) samples, demonstrating the strong impact of the Cl-coordination on the intrinsic activity (Figure 3e).

Furthermore, the double-layer capacitance (C_{dl}), which is related to the electrochemically active surface area of the electrocatalyst, was obtained from CV curves at different scan rates in the nonfaradaic region. The C_{dl} value of the FePc-Cl-CNTs catalyst is determined to be 22.89 mF cm^{-2}, being significantly higher than that of the FePc-CNTs (11.52 mF cm^{-2}) and Pt/C samples (10.9 mF cm^{-2}) (Figure S22). From these results, it can be concluded that Cl-coordination enlarges the electrochemical reaction area, ensuring to expose more active sites. The higher C_{dl} value indicates that the material possesses a greater abundance of electron transport channels, ensuring to deliver enhanced electrocatalytic activities. Besides catalytic activity, the stability is another critical factor from the perspective of practical applications. After 3000 cycles durability test (ADT), negligible decline of $E_{1/2}$ was observed in FePc-Cl-CNTs, being superior to those of FePc-CNTs (11 mV) and Pt/C (18 mV) (Figures 3f, S23, and S24).

The robust stability nature of the as-prepared FePc-Cl-CNTs could also be validated from the amperometry testing. After 65 000 s testing, a 15% current loss was recorded for the FePc-Cl-CNTs catalyst, whereas FePc-CNTs and Pt/C samples experienced 32% and 46.3% (counted to 45000 s) current loss, respectively (Figures 3g and S25). Meanwhile, we performed a comprehensive assessment of iron consumption using CV and ICP-OES analysis. As illustrated in Figure S26, after 5000 CV cycles, the iron consumption rate in FePc-Cl-CNTs was maintained at 5.17%. In contrast, under the same experimental conditions, the consumption rate of FePc-CNTs was significantly higher, being up to 10.42%. This pronounced difference indicates that the strategic addition of chlorine effectively mitigates the leaching of iron, thereby substantially enhancing the structural stability and electrocatalytic durability of the catalyst. Also, the XPS results for C 1s and Cl 2p do not exhibit significant changes after the reaction. (Figure S27) Additionally, a methanol crossover

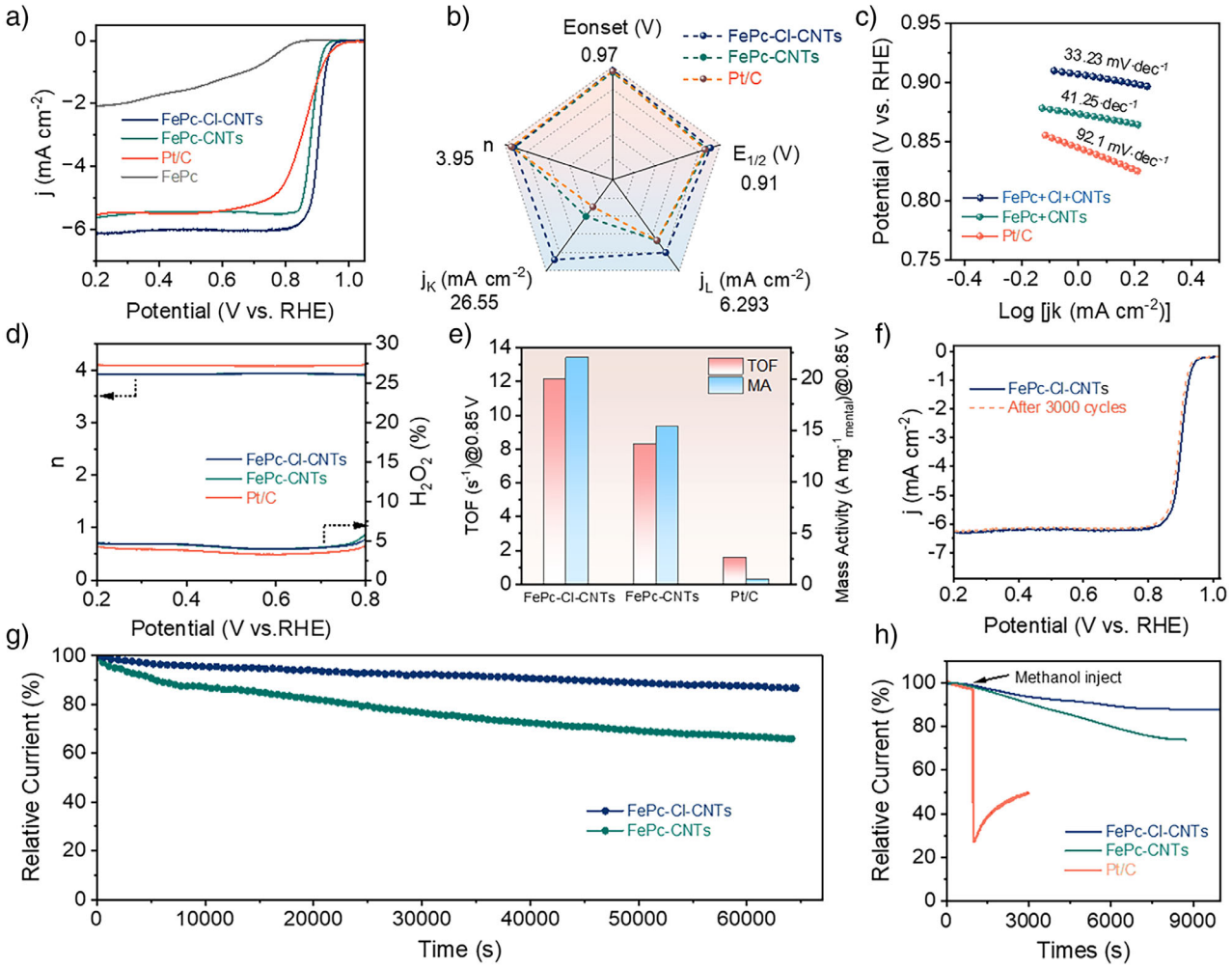

Figure 3. Electrocatalytic ORR performance of the catalyst. a) LSV curves of FePc-Cl-CNTs and the control samples measured in 0.1 M KOH solutions. b) Radar map describing E_{onset}, $E_{1/2}$, limiting current density (J_L), kinetic current density (J_K), and Tafel slope. c) Tafel slopes. d) Electron transfer number of the samples measured in 0.1 M KOH. e) Mass activity and TOF values of Fe—N_4 sites of FePc-Cl-CNTs and FePc-CNTs. f) LSV curves before and after 3000 potential cycles (0.6–1.0 V versus RHE). g) *i–t* curves of FePc-Cl-CNTs and Pt/C measured in 0.1 M KOH. h) Methanol crossover tolerance behaviors of FePc-Cl-CNTs and Pt/C.

poisoning evaluation was conducted as well. As expected, no significant current drop was observed after 3 M methanol introduction for the FePc-Cl-CNTs catalyst, outperforming the control FePc-CNTs sample as well as Pt/C which is seriously poisoned. This behavior indicates that the FePc-Cl-CNTs catalyst possesses excellent methanol tolerance and is a good candidate for practical ORR applications (Figures 3h and S28).

Zn–Air Batteries Analysis

Encouraged by the addressed excellent electrocatalytic performance, a self-assembled zinc–air batteries (ZABs) was configured with FePc-Cl-CNTs and Zn plate serving as cathode and anode, respectively. The schematic illustration of our fabricated ZABs is depicted in Figure 4a. The open-circuit voltage (OCV) of the our FePc-Cl-CNTsIIZn is up to 1.51 V, which is close to the theoretical value of 1.65 V and superior to that of the Pt/CIIZn, for which the OCV is recorded to be 1.44 V (Figures 4b and S29). The as-fabricated ZABs exhibited a higher discharge current density and a larger charge–discharge voltage gap when compared to Pt/CIIZn (Figure 4c). Furthermore, the ZABs exhibited a maximum power density of 183.5 mW cm^{-2}, surpassing that of the Pt/CIIZn, which attained only 108.5 mW cm^{-2} (Figure 4d). At a fixed discharge current density of 20 mA cm^{-2}, the FePc-Cl-CNTsIIZn yields a specific capacity of 797.16 mAh gZn^{-1}, which is superior to that of Pt/CIIZn (737.15 mAh gZn^{-1}) (Figure 4e). Furthermore, we also evaluated the stability of our as-fabricated ZABs. No significant decay was observed during testing across the current density range of 2–100 mA cm^{-2} (Figure 4f). When the current density was reduced to 2 mA cm^{-2}, the discharging voltage can be successfully restored back to high value. Apart from the disposable ZABs, a rechargeable ZABs was further assembled using a composite catalyst composed of FePc-Cl-CNTs and RuO_2 (with 1:1 mass ratio) for long-term durability testing. In the

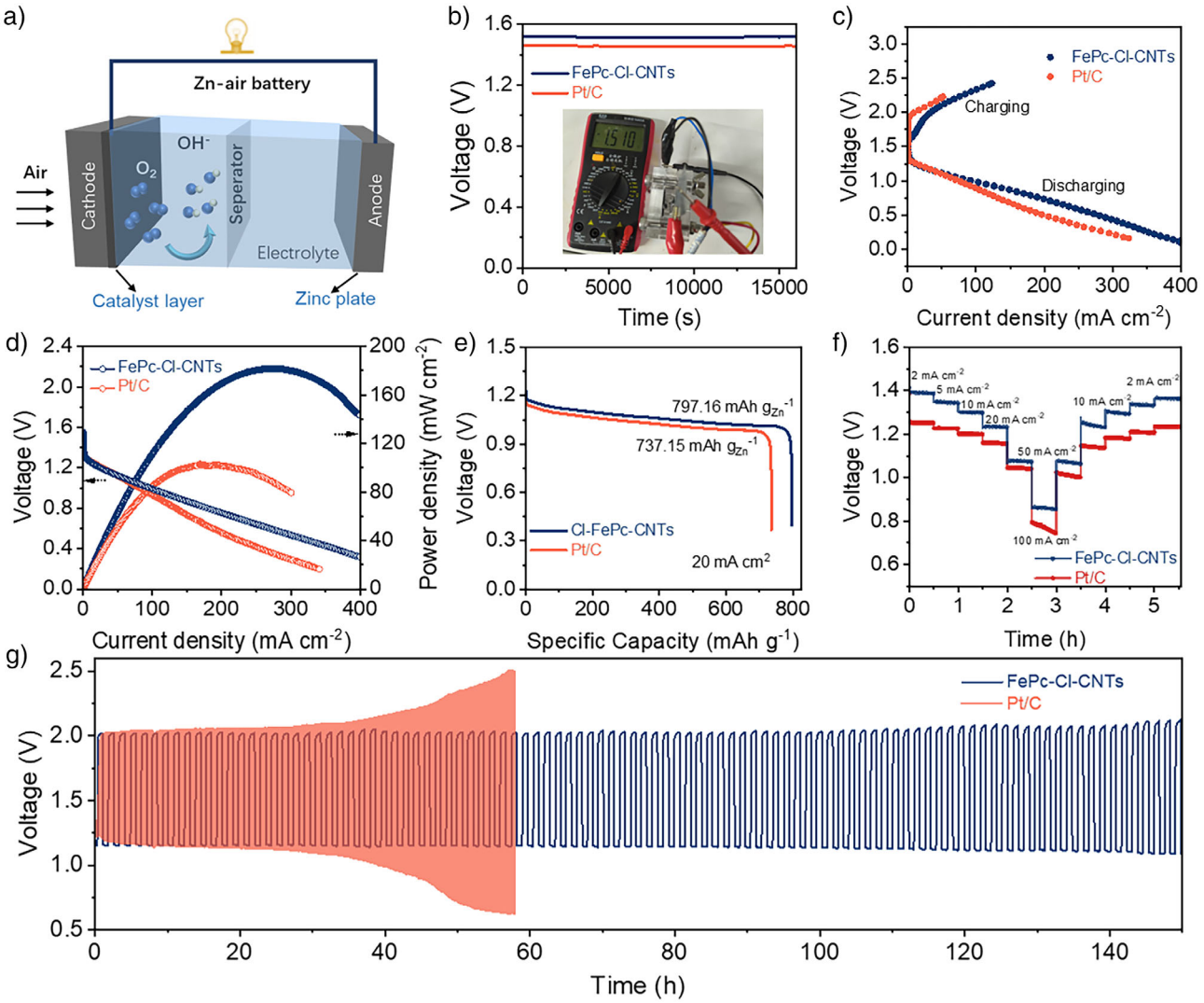

Figure 4. Performance of zinc–air battery. a) Schematic illustration of the configured zinc–air battery. b) Open-circuit voltage of FePc-Cl-CNTs-based and Pt/C-based ZABs. c) Charge discharge polarization curves of the samples. d) Discharge–polarization curves and the corresponding power density curves. e) Galvanostatic discharge curves at 20 mA cm^{-2}. f) Rate capability test of Zn–air batteries using FePc-Cl-CNTs and Pt/C catalysts at different current densities. g) Galvanostatic discharge/charge cycling performance of rechargeable ZABs based on FePc-Cl-CNTs + RuO_2 and Pt/C + RuO_2 at 5 mA cm^{-2}.

galvanostatic charge–discharge cycling measurement, each cycle lasts for one hour (0.5 h discharging followed by 0.5 h charging) at a constant current density of 5 mA cm^{-2}. Impressively, FePc-Cl-CNTs + RuO_2-based ZABsIIZn demonstrated robust stability for over 150 h (Figure 4g). For comparison, another rechargeable ZABs of Pt/C + RuO_2 was also constructed. Significant performance decay can be observed after ~20 h working under the same test conditions. These cycling behaviors further demonstrate the advanced nature of our designed FePc-Cl-CNTs under alkaline condition, evidencing its feasibility for practical ZABs applications.

Mechanistic Insights

To further clarify the impact of axial Cl on the coordination environment and catalytic mechanism as well as elucidate the excellent oxygen reduction activity of the FePc-Cl-CNTs catalyst, DFT calculations were performed. The utilized structural models of FePc-Cl-CNTs and FePc-CNTs for DFT calculation were constructed following the XPS and XAS findings. Due to π–π interactions between FePc and CNTs in FePc-CNTs, FePc is slightly curved but maintains an overall planar symmetric structure, with similar Fe—N bond lengths (Figure S30). In more detail, Fe—N (1) and Fe—N (2) lengths are 1.931 Å, and Fe—N (3) and Fe—N (4) lengths are 1.932 Å, being consistent with its D_{4h} symmetry. Noteworthy, after axial Cl atom coordination, the FePc-Cl-CNTs sample revealed different structural features, by which it can be identified that the mediating effect of Cl atoms significantly reduced the symmetry of FePc and caused obvious distortion of the geometric structure of the Fe centers. Interestingly, compared to the D_{4h} symmetry of FePc-CNTs, the average Fe—N bond length in FePc-Cl-CNTs is slightly extended (the

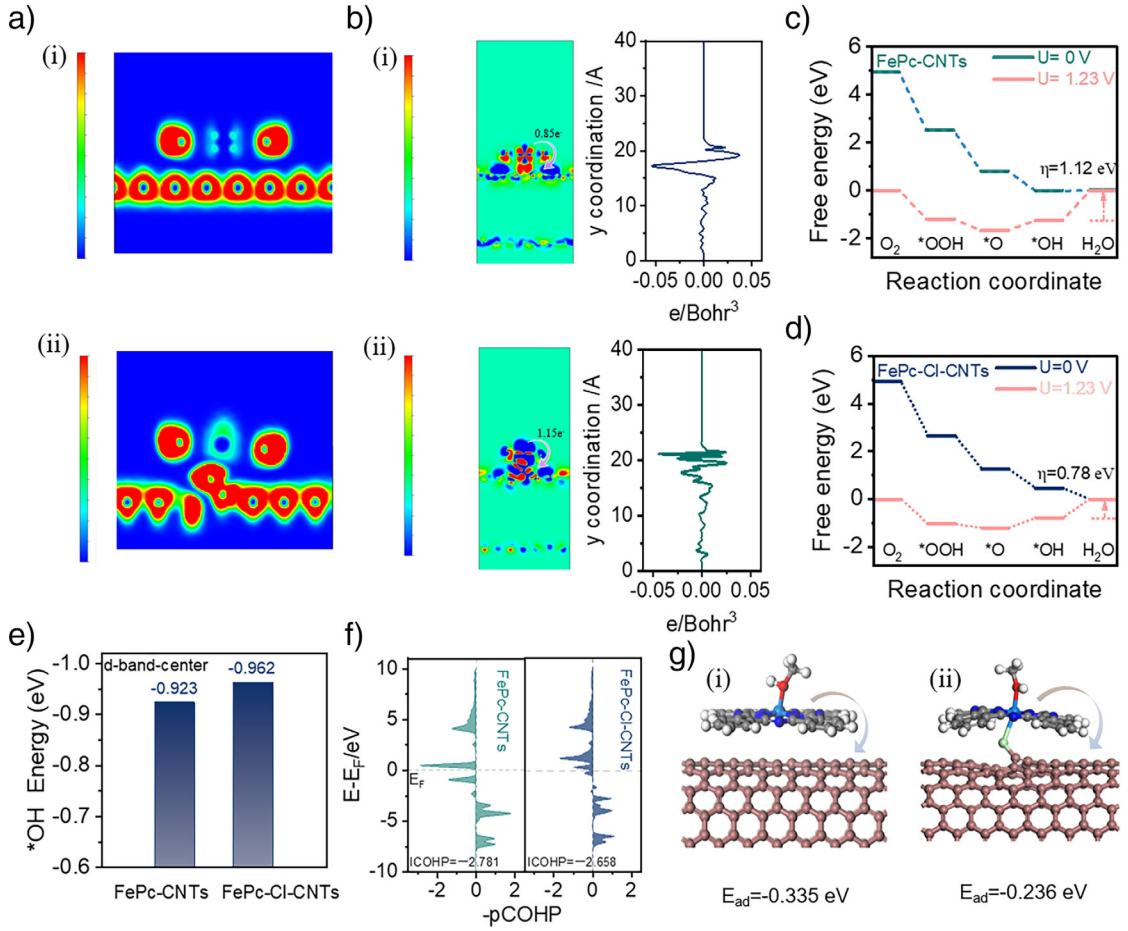

Figure 5. DFT calculations. a) Electron localization function of (i) FePc-CNTs and (ii) FePc-Cl-CNTs. Scale bar, 0–1. b) Differential charge density and the corresponding planar average charge density of (i) FePc-CNTs and (ii) FePc-Cl-CNTs, scale bar, −0.1–0.1. c, d) ORR free energy diagram of FePc-CNTs and FePc-Cl-CNTs at different electrode potentials. e) d band center plot of FePc-CNTs and FePc-Cl-CNTs. f) COHP and ICOHP between Fe-O of FePc-CNTs and FePc-Cl-CNTs. g) Adsorption energy (E_{ads}) of methanol molecules on FePc-CNTs and FePc-Cl-CNTs.

detailed bond length variation is listed in Table S7). As Fe—N (4) is significantly elongated, an asymmetric coordination environment is favored (Figure S31). Such variation could be attributed to the electronegative nature of Cl, leading to a weakened covalent bond strength of Fe—N.[56] It is important to note that, appropriate Fe—N bond lengths are crucial for preventing the aggregation and shedding of Fe atoms, thereby achieving effective metal atom dispersion and anchoring.[57–60]

Electron localization function (ELF) of FePc-CNTs and FePc-Cl-CNTs was subsequently calculated to more vividly display the electronic structure of the materials. As shown in Figure 5a(i), a highly symmetric charge distribution is revealed for FePc-CNTs, representing its characteristic planar Fe—N_4 configuration. In contrast, asymmetric electron distribution along the axis direction is observed after axial Cl atoms coordination in the matrix (Figure 5a(ii)), by which it is evidenced that Cl atoms induce strong electron localization states and is the intrinsic reason for the electronic structure reconstruction. Differential charge density and the corresponding planar average charge density calculation further reveal the essence of this change (Figure S32). In symmetric FePc-CNTs, the interaction between FePc and CNTs is relatively weak (Figure 5b(i)). Nonetheless, the axial-coordinated Cl atoms in FePc-Cl-CNTs alter the charge transfer pattern through interactions with Fe metal sites in FeN_4, forming a pronounced charge transfer distribution in the axial region (Figure 5b(ii)). To precisely quantify the electron transfer, Bader charge analysis was employed. The Bader charge transfer of the Fe center is $-0.85e^-$ in FePc-CNTs. Because of the symmetry breaking of electron density near FeN_4 with the introduction of Cl atoms, the Bader charge transfer of Fe center increases to $-1.15e^-$ in FePc-Cl-CNTs, signifying the increase of the valence state of Fe, being consistent with the aforementioned DFT results as well XAS results shown in Figure 2f. The free energy of each ORR step on FePc-CNTs and FePc-Cl-CNTs was calculated, the utilized atomic models are demonstrated in Figures S33 and S34. Figure 5c,d show the ORR free energy diagram of FePc-CNTs and FePc-Cl-CNTs, in which it can be found that the rate-determining step (RDS) for ORR on both samples is the desorption of *OH.[61]

By careful scrutinizing the data, it can be identified that the overpotential is lowered to 0.78 eV after the introduction of axial Cl ligands (versus 1.12 eV for Cl-free one), signifying

that the presence of Cl ligands weakens the *OH desorption affinity. To further understand the mechanism how axial ligands influence *OH adsorption as well as to quantify the electronic bonding/antibonding states, projected density of states (PDOS) and crystal orbital Hamilton population (COHP) calculations were carried out. The PDOS plots of Fe d orbitals and *OH p orbitals are shown in Figures 5e and S35, yielding d band centers of −0.923 and −0.962 eV for FePc-CNTs and FePc-Cl-CNTs, respectively. It shows that the presence of axial Cl leads to a lowered d band center of FePc-Cl-CNTs, in which it weakens the *OH adsorption capacity and facilitates the desorption. From the further collected integrated COHP (ICOHP) values, it quantifies that the Fe─O bonding in FePc-CNTs and FePc-Cl-CNTs are −2.781 and −2.685 eV, respectively. The reduced strength of the Fe─O bonding suggests that the introduction of axial Cl effectively facilitates the desorption of the *OH intermediate (Figure 5e), ensuring charge transfer from the Fe center to the adjacent N atoms.

In order to examine the antipoisoning properties of FePc-CNTs and FePc-Cl-CNTs theoretically, the adsorption energy of methanol (E_{ads}) on the two samples was calculated as well. As shown in Figure 5g, E_{ads} of FePc-CNTs and FePc-Cl-CNTs were determined to be −0.335 and −0.236 eV, respectively. The weaker methanol adsorption feature of FePc-Cl-CNTs supports the statement that the introduction of Cl effectively inhibits the adsorption of active small molecules, which could be the reason for the delivered excellent methanol tolerance, being consistent with the experimental observation shown in Figure 3h.

Conclusion

In summary, a "Cl-mediation" strategy is designed and adopted to break the symmetry of Fe–N–C, in which axial Cl atoms are coordinated to FePc molecules on CNTs matrix. XAS measurement unveils that the axial Cl atoms enlarge the Fe─N bond length in the disrupted planar conjugated structure, inducing a transformation of Fe─N_4 from D_{4h} to C_{4v} symmetry. The tuned geometric configuration of Fe─N_4 mitigates the dissolution of Fe centers during the catalytic process, thereby yielding robust ORR activity. The effect of Cl-mediation on Fe–N–C is further validated from the testing of a configured Zn–air battery, yielding remarkable power density and specific capacity (183.5 mW cm^{-2} and 797.16 mAh gZn^{-1} versus 108.5 mW cm^{-2} and 737.15 mAh gZn^{-1} of Pt/C-based one) as well as robust stability for over 150 h working duration. DFT calculations clarify that axial Cl atoms reshape electron-cloud distribution around the Fe centers and effectively lower the ORR energy barriers, subsequently optimizing the *OH desorption and suppressing poisonous molecule adsorption.

Supporting Information

The authors have cited additional references within the Supporting Information for mass activity (MA)[62] and DFT calculation method.[63–67]

Acknowledgements

This work is financially supported by the National Natural Science Foundation of China (Grants No. 52272202 and W2421027). R.S. would like to acknowledge the Excellence of Science FWO-FNRS project (PLASyntH2, FNRS grant O.0023.22, EOS ID: 40007511). The authors would extend thanks to the staff of beamline BL13SSW at Shanghai Synchrotron Radiation Facility (SSRF) for providing the beam time and the experimental support. M.H., M.B., and C.W. would like to acknowledge Prince Sultan University. The computation is completed in the HPC Platform of Huazhong University of Science and Technology.

Conflict of Interests

The authors declare no conflict of interest.

Data Availability Statement

The data that support the findings of this study are available from the corresponding author upon reasonable request.

Keywords: Axial Cl-mediation · Fe–N–C · FePc molecules · Oxygen reduction reaction · Zinc–air batteries

[1] Y. Wang, J. Wu, S. Tang, J. Yang, C. Ye, J. Chen, Y. Lei, D. Wang, *Angew. Chem. Int. Ed.* **2023**, *62*, e202219191.
[2] K. Wang, Z. Lu, J. Lei, Z. Liu, Y. Li, Y. Cao, *ACS Nano* **2022**, *16*, 11944–11956.
[3] D. Du, S. Zhao, Z. Zhu, F. Li, J. Chen, *Angew. Chem. Int. Ed.* **2020**, *59*, 18140–18144.
[4] R. Zhuang, P. Wang, L. Wang, Q. Lai, J. Qiu, Y. Chen, X. Zhang, L. Sun, Y. Hua, *Angew. Chem. Int. Ed.* **2024**, e202413660.
[5] Y. Chen, S. Ji, S. Zhao, W. Chen, J. Dong, W. C. Cheong, R. Shen, X. Wen, L. Zheng, A. I. Rykov, S. Cai, H. Tang, Z. Zhuang, C. Chen, Q. Peng, D. Wang, Y. Li, *Nat. Commun.* **2018**, *9*, 5422.
[6] M. K. Debe, *Nature* **2012**, *486*, 43–51.
[7] Y. Zhou, Z. Xie, J. Jiang, J. Wang, X. Song, Q. He, W. Ding, Z. Wei, *Nat. Catal.* **2020**, *3*, 454–462.
[8] S. Ponnada, M. S. Kiai, D. B. Gorle, A. Nowduri, R. K. Sharma, *Energy Fuels* **2021**, *35*, 15265–15284.
[9] L. Wang, J. Wu, S. Wang, H. Liu, Y. Wang, D. Wang, *Nano Res.* **2024**, *17*, 3261–3301.
[10] A. Han, W. Sun, X. Wan, D. Cai, X. Wang, F. Li, J. Shui, D. Wang, *Angew. Chem. Int. Ed.* **2023**, *62*, e202303185.
[11] Z. Miao, S. Li, C. Priest, T. Wang, G. Wu, Q. Li, *Adv. Mater.* **2022**, *34*, e2200595.
[12] L. Jiao, J. Li, L. L. Richard, Q. Sun, T. Stracensky, E. Liu, M. T. Sougrati, Z. Zhao, F. Yang, S. Zhong, H. Xu, S. Mukerjee, Y. Huang, D. A. Cullen, J. H. Park, M. Ferrandon, D. J. Myers, F. Jaouen, Q. Jia, *Nat. Mater.* **2021**, *20*, 1385–1391.
[13] L. J. Liu, Z. Y. Wang, Z. Y. Wang, R. Wang, S. Q. Zang, T. C. W. Mak, *Angew. Chem. Int. Ed.* **2022**, *61*, e202205626.
[14] L. Lu, S. Zou, B. Fang, *ACS Catal.* **2021**, *11*, 6020–6058.
[15] H. Zhang, H. C. Chen, S. Feizpoor, L. Li, X. Zhang, X. Xu, Z. Zhuang, Z. Li, W. Hu, R. Snyders, D. Wang, C. Wang, *Adv. Mater.* **2024**, *36*, e2400523.

[16] H. Sun, C. W. Tung, Y. Qiu, W. Zhang, Q. Wang, Z. Li, J. Tang, H. C. Chen, C. Wang, H. M. Chen, *J. Am. Chem. Soc.* **2022**, *144*, 1174–1186.
[17] J. Qiao, C. Lu, L. Kong, J. Zhang, Q. Lin, H. Huang, C. Li, W. He, M. Zhou, Z. Sun, *Adv. Funct. Mater.* **2024**, *34*, 2409794.
[18] Z. D. Wang, Y. Han, Y. Y. Wang, S. Q. Zang, P. Peng, *Angew. Chem. Int. Ed.* **2024**, *64*, e202416973.
[19] B. Huang, L. Li, X. Tang, W. Zhai, Y. Hong, T. Hu, K. Yuan, Y. Chen, *Energy Environ. Sci.* **2021**, *14*, 2789–2808.
[20] P. Peng, L. Shi, F. Huo, C. Mi, X. Wu, S. Zhang, Z. Xiang, *Sci Adv.* **2019**, *5*, eaaw2322.
[21] J. Chen, J. Huang, R. Wang, W. Feng, H. Wang, T. Luo, Y. Hu, C. Yuan, L. Feng, L. Cao, K. Kajiyoshi, C. He, Y. Liu, Z. Li, Y. Feng, *Chem. Eng. J.* **2022**, *441*, 136078.
[22] L. Hu, C. Dai, L. Chen, Y. Zhu, Y. Hao, Q. Zhang, L. Gu, X. Feng, S. Yuan, L. Wang, B. Wang, *Angew. Chem. Int. Ed.* **2021**, *60*, 27324–27329.
[23] R. Cao, R. Thapa, H. Kim, X. Xu, M. Gyu Kim, Q. Li, N. Park, M. Liu, J. Cho, *Nat. Commun.* **2013**, *4*, 2076.
[24] R. Baker, D. P. Wilkinson, J. Zhang, *Electrochim. Acta* **2008**, *53*, 6906–6919.
[25] X. Wang, B. Wang, J. Zhong, F. Zhao, N. Han, W. Huang, M. Zeng, J. Fan, Y. Li, *Nano Res.* **2016**, *9*, 1497–1506.
[26] Z.y. Mei, S. Cai, G. Zhao, X. Zou, Y. Fu, J. Jiang, Q. An, M. Li, T. Liu, H. Guo, *Chem. Eng. J.* **2022**, *430*, 132691.
[27] J. Wang, X. Huang, S. Xi, H. Xu, X. Wang, *Angew. Chem. Int. Ed.* **2020**, *59*, 19162–19167.
[28] L. Sun, X. Jin, T. Su, A. C. Fisher, X. Wang, *Adv. Mater.* **2024**, *36*, e2306336.
[29] L. Sun, Z. Huang, V. Reddu, T. Su, A. C. Fisher, X. Wang, *Angew. Chem. Int. Ed.* **2020**, *59*, 17104–17109.
[30] J. Su, C. B. Musgrave, Y. Song, L. Huang, Y. Liu, G. Li, Y. Xin, P. Xiong, M. M.J. Li, H. Wu, M. Zhu, H. M. Chen, J. Zhang, H. Shen, B. Z. Tang, M. Robert, W. A. Goddard, R. Ye, *Nat. Catal.* **2023**, *6*, 818–828.
[31] Y. Dai, B. Liu, Z. Zhang, P. Guo, C. Liu, Y. Zhang, L. Zhao, Z. Wang, *Adv. Mater.* **2023**, *35*, e2210757
[32] X. Tang, Y. Wei, W. Zhai, Y. Wu, T. Hu, K. Yuan, Y. Chen, *Adv. Mater.* **2023**, *35*, e2208942.
[33] C. Liu, Z. Yu, F. She, J. Chen, F. Liu, J. Qu, J. M. Cairney, C. Wu, K. Liu, W. Yang, H. Zheng, Y. Chen, H. Li, L. Wei, *Energy Environ. Sci.* **2023**, *16*, 446–459.
[34] S. Xu, Y. Ding, J. Du, Y. Zhu, G. Liu, Z. Wen, X. Liu, Y. Shi, H. Gao, L. Sun, F. Li, *ACS Catal.* **2022**, *12*, 5502–5509.
[35] S. Zhu, L. Ding, X. Zhang, K. Wang, X. Wang, F. Yang, G. Han, *Angew. Chem. Int. Ed.* **2023**, *62*, e202309545.
[36] F. Kong, X. Cui, Y. Huang, H. Yao, Y. Chen, H. Tian, G. Meng, C. Chen, Z. Chang, J. Shi, *Angew. Chem. Int. Ed.* **2022**, *61*, e202116290.
[37] J. Yang, W. H. Li, H. T. Tang, Y. M. Pan, D. Wang, Y. Li, *Nature* **2023**, *617*, 519–523.
[38] X. Feng, G. Chen, Z. Cui, R. Qin, W. Jiao, Z. Huang, Z. Shang, C. Ma, X. Zheng, Y. Han, W. Huang, *Angew. Chem. Int. Ed.* **2024**, *63*, e202316314.
[39] Q. Wang, Y. Yang, F. Sun, G. Chen, J. Wang, L. Peng, W. T. Chen, L. Shang, J. Zhao, D. Sun-Waterhouse, T. Zhang, G. I. N. Waterhouse, *Adv. Energy Mater.* **2021**, *11*, 2100219.
[40] Y. Cao, Z. Liu, Y. Tang, C. Huang, Z. Wang, F. Liu, Y. Wen, B. Shan, R. Chen, *Carbon* **2021**, *180*, 1–9.
[41] C. Zhang, W. Shen, K. Guo, M. Xiong, J. Zhang, X. Lu, *J. Am. Chem. Soc.* **2023**, *145*, 11589–11598.
[42] S. Liu, Y. Zhang, B. Ge, F. Zheng, N. Zhang, M. Zuo, Y. Yang, Q. Chen, *Adv. Mater.* **2021**, *33*, e2103133.
[43] J. Zhu, Y. Huang, W. Mei, C. Zhao, C. Zhang, J. Zhang, I. S. Amiinu, S. Mu, *Angew. Chem. Int. Ed.* **2019**, *58*, 3859–3864.
[44] J. Gao, Y. Wang, H. Wu, X. Liu, L. Wang, Q. Yu, A. Li, H. Wang, C. Song, Z. Gao, M. Peng, M. Zhang, N. Ma, J. Wang, W. Zhou, G. Wang, Z. Yin, D. Ma, *Angew. Chem. Int. Ed.* **2019**, *58*, 15089–15097.
[45] M. F. Sanad, H. M. Franklin, B. A. Ali, A. R. Puente Santiago, A. N. Nair, V. S. N. Chava, O. Fernandez-Delgado, N. K. Allam, S. Stevenson, S. T. Sreenivasan, L. Echegoyen, *Angew. Chem. Int. Ed.* **2022**, *61*, e202116727.
[46] G. Ye, S. Liu, K. Zhao, Z. He, *Angew. Chem. Int. Ed.* **2023**, *62*, e202303409.
[47] X. Tan, J. Zhang, F. Cao, Y. Liu, H. Yang, Q. Zhou, X. Li, R. Wang, Z. Li, H. Hu, Q. Zhao, M. Wu, *Adv. Sci.* **2024**, *11*, e2306599.
[48] Z.-y. Mei, S. Cai, G. Zhao, Q. Jing, X. Sheng, J. Jiang, H. Guo, *Energy Storage Mater.* **2022**, *50*, 12–20.
[49] B. Tang, Q. Ji, X. Zhang, R. Shi, J. Ma, Z. Zhuang, M. Sun, H. Wang, R. Liu, H. Liu, C. Wang, Z. Guo, L. Lu, P. Jiang, D. Wang, W. Yan, *Angew. Chem. Int. Ed.* **2025**, *137*, e202424135.
[50] W. Xu, R. Zeng, M. Rebarchik, A. Posada-Borbon, H. Li, C. J. Pollock, M. Mavrikakis, H. D. Abruna, *J. Am. Chem. Soc.* **2024**, *146*, 2593–2603.
[51] H. Peng, W. Wang, J. Gao, F. Jiang, B. Li, Y. Wang, Y. Wu, Y. Wang, J. Li, J. Peng, W. Hu, Z. Wen, D. Wang, E. Zhang, M. Zhai, *Adv. Sci.* **2024**, *12*, e2411928.
[52] K. Chen, K. Liu, P. An, H. Li, Y. Lin, J. Hu, C. Jia, J. Fu, H. Li, H. Liu, Z. Lin, W. Li, J. Li, Y. R. Lu, T. S. Chan, N. Zhang, M. Liu, *Nat. Commun.* **2020**, *11*, 4173.
[53] Q. Jia, N. Ramaswamy, H. Hafiz, U. Tylus, K. Strickland, G. Wu, B. Barbiellini, A. Bansil, E. F. Holby, P. Zelenay, S. Mukerjee, *ACS Nano* **2015**, *9*, 12496–12505.
[54] A. V. Soldatov, G. Smolentsev, A. Kravtsova, G. Yalovega, M. C. Feiters, G. A. Metselaar, Y. Joly, *Radiat. Phys. Chem.* **2006**, *75*, 1866–1868.
[55] S. Grenier, Y. Joly, *J. Phys. Conf. Ser.* **2014**, *519*, 012001.
[56] G. Chen, R. Lu, C. Li, J. Yu, X. Li, L. Ni, Q. Zhang, G. Zhu, S. Liu, J. Zhang, U. I. Kramm, Y. Zhao, G. Wu, J. Xie, X. Feng, *Adv. Mater.* **2023**, *35*, e2300907.
[57] Q. Ma, H. Jin, J. Zhu, Z. Li, H. Xu, B. Liu, Z. Zhang, J. Ma, S. Mu, *Adv. Sci.* **2021**, *8*, e2102209.
[58] H. Li, S. Di, P. Niu, S. Wang, J. Wang, L. Li, *Energy Environ. Sci.* **2022**, *15*, 1601–1610.
[59] Y. Ma, J. Li, X. Liao, W. Luo, W. Huang, J. Meng, Q. Chen, S. Xi, R. Yu, Y. Zhao, L. Zhou, L. Mai, *Adv. Funct. Mater.* **2020**, *30*, 2005000.
[60] X. Zhang, Z. Wu, X. Zhang, L. Li, Y. Li, H. Xu, X. Li, X. Yu, Z. Zhang, Y. Liang, H. Wang, *Nat. Commun.* **2017**, *8*, 14675.
[61] Y. Li, R. Hu, Z. Chen, X. Wan, J.-X. Shang, F.-H. Wang, J. Shui, *Nano Res.* **2021**, *14*, 611–619.
[62] Y. F. Xia, P. Guo, J. Z. Li, L. Zhao, X. L. Sui, Y. Wang, Z. B. Wang, *iScience* **2021**, *24*, 103024.
[63] G. Kresse, J. Furthmüller, *Comput. Mater. Sci.* **1996**, *6*, 15–50.
[64] G. Kresse, J. Hafner, *Phys. Rev. B Condens. Matter* **1993**, *47*, 558–561.
[65] P. E. Blochl, *Phys. Rev. B Condens. Matter* **1994**, *50*, 17953–17979.
[66] B. Hammer, L. B. Hansen, J. K. Nørskov, *Phys. Rev. B* **1999**, *59*, 7413–7421.
[67] J. P. Perdew, J. A. Chevary, S. H. Vosko, K. A. Jackson, M. R. Pederson, D. J. Singh, C. Fiolhais, *Phys. Rev. B Condens. Matter* **1992**, *46*, 6671–6687.

Manuscript received: March 01, 2025
Revised manuscript received: April 14, 2025
Accepted manuscript online: April 15, 2025
Version of record online: April 24, 2025